

# A spine-sheath model for strong-line blazars

Marek Sikora,<sup>1</sup>★ Mieszko Rutkowski,<sup>2</sup> and Mitchell C. Begelman<sup>3,4</sup>

<sup>1</sup>*Nicolaus Copernicus Astronomical Center, Bartycka 18, 00-716 Warsaw, Poland*

<sup>2</sup>*Marian Smoluchowski Institute of Physics, Jagiellonian University, Lojasiewicza 11, 30-348 Cracow, Poland*

<sup>3</sup>*JILA, University of Colorado and National Institute of Standards and Technology, 440 UCB, Boulder, CO 80309, USA*

<sup>4</sup>*Department of Astrophysical and Planetary Sciences, University of Colorado, 391 UCB, Boulder, CO 80309, USA*

## ABSTRACT

We have developed a quasi-analytical model for the production of radiation in strong-line blazars, assuming a spine-sheath jet structure. The model allows us to study how the spine and sheath spectral components depend on parameters describing the geometrical and physical structure of “the blazar zone”. We show that typical broad-band spectra of strong-line blazars can be reproduced by assuming the magnetization parameter to be of order unity and reconnection to be the dominant dissipation mechanism. Furthermore, we demonstrate that the spine-sheath model can explain why gamma-ray variations are often observed to have much larger amplitudes than the corresponding optical variations. The model is also less demanding of jet power than one-zone models, and can reproduce the basic features of extreme  $\gamma$ -ray events.

**Key words:** quasars: jets — radiation mechanisms: non-thermal — acceleration of particles

## 1 INTRODUCTION

Given the complexity of AGN jet physics (e.g., Begelman et al. 1984), one may be surprised by the success of one-zone, homogeneous models in fitting observed blazar spectra (see Ghisellini et al. 2014 and refs. therein). In large part, this success is due to the fact that most blazar radiation is emitted in very localized regions. This is indicated by the time scales of variations and their correlations between different spectral bands. In the case of blazars associated with flat-spectrum radio quasars (FSRQs), such correlations are found to be particularly strong between optical and  $\gamma$ -ray variations ((Bonning et al. 2012; Cohen et al. 2014; Hovatta et al. 2014)). This implies co-spatial production of low- and high-energy spectral components, the former assumed to be emitted by the synchrotron mechanism, the latter most likely produced by the external-radiation Compton (ERC) process (Sikora et al. 2009 and refs. therein). Sometimes, however, the  $\gamma$ -ray flux variations — particularly during higher states — have much larger fractional amplitudes than the optical variations (Wehrle et al. 1998; Marscher et al. 2010; Vercellone et al. 2011; Ackermann et al. 2014; Cohen et al. 2014; Carnerero et al. 2015; Hayashida et al. 2015), which is difficult to explain if both spectral components are produced by the same population of relativistic electrons. This situation is likely to result from contamination of the optical radiation produced co-spatially with  $\gamma$ -rays by slowly-varying radiation from another region in the jet. In order to avoid simultaneous contamination (and suppression) of the  $\gamma$ -ray variations, the contaminating source in this region should have a lower bulk Lorentz factor  $\Gamma$  and/or higher

comoving magnetic field  $B$  than the bursting region. (This is because the ERC-to-synchrotron luminosity ratio,  $L_{\text{ERC}}/L_{\text{syn}}$ , is proportional to  $\Gamma^2/B^2$ ). We assume that such a source is associated with slower moving sheaths/layers of laterally stratified jets.

Spine-sheath structures, with a spine moving faster than the sheath, have already been investigated in the context of astrophysical jet phenomenology (Sol et al. 1989; Celotti et al. 2001; Ghisellini et al. 2005; Tavecchio & Ghisellini 2008; D’arcangelo et al. 2009; Mimica et al. 2015; Janiak et al. 2015a). Their MHD structure was investigated by Bogovalov & Tsinganos (2005), Gracia et al. (2005), Nishikawa et al. (2005), Mizuno et al. (2007), and Beskin & Nokhrina (2006), and their stability conditions were analyzed by Hardee (2007) and Hardee et al. (2007). So far, the spine-sheath model has not been worked out in detail for blazars with dense radiative environments, where ERC is the dominant radiation process. In particular, it has not been determined how significant a contribution Comptonization of synchrotron radiation emitted in the sheath can make to  $\gamma$ -ray production in the spine. In this paper we present a model that allows us to make analytic estimates of all spine and sheath spectral components and their dependence on such parameters as powers, magnetizations, opening angles and bulk Lorentz factors. The spine-sheath model and its basic assumptions are introduced in section 2; the approximate formulae allowing calculation of luminosities and frequencies of different spectral components are presented in sections 2.1 and 2.2, respectively; and the dependence of these luminosities and frequencies on the viewing angle are illustrated for an exemplary model in section 3. In sections 4.1–4.4 we discuss how the spine-sheath model can resolve several problems that afflict one-zone models for spectra and variability of strong-line blazars, and summarize the main results in section 4.5.

★ Contact e-mail: sikora@camk.edu.pl

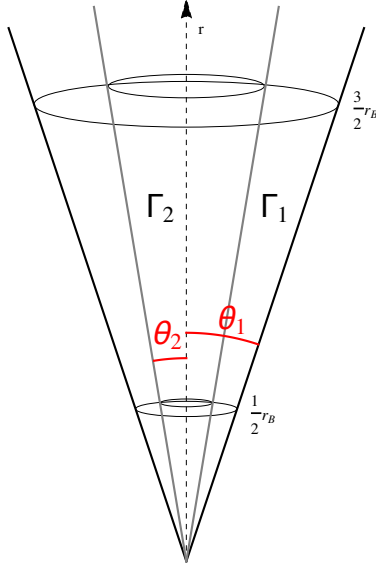


**Figure 1.** Scheme of the spine-sheath structure of a jet.

## 2 SPINE-SHEATH MODEL

We assume that the jet has the “spine-sheath” conical geometry (see 1), in which the Lorentz factor of the spine,  $\Gamma_2$ , is much larger than that of the sheath,  $\Gamma_1$ . The spine and sheath each possess an “active” zone, where most of blazar radiation is produced, within the same distance range  $r_{\text{bl}}/2 < r < 3r_{\text{bl}}/2$ . Just prior to the active zone the powers of both jet components are dominated by a sum of the magnetic energy flux,  $L_{B0,i}$ , and the kinetic energy flux of cold protons,  $L_{p0,i}$ . These powers, expressed as a function of the mass flux,  $\dot{M}$ , and magnetization,  $\sigma_{0,i} \equiv L_{B0,i}/L_{p0,i}$ , are

$$P_{0,i} = L_{B0,i} + L_{p0,i} = (1 + \sigma_{0,i})(\Gamma_{0,i} - 1)\dot{M}_p c^2, \quad (1)$$

while magnetic energy fluxes are

$$L_{B0,i} = \frac{\sigma_{0,i}}{1 + \sigma_{0,i}} P_{0,i}, \quad (2)$$

where  $i = 1, 2$ . We assume that steady-state, axisymmetric jets can dissipate their energy via magnetic reconnection, as well as in reconfinement shocks. The efficiency of dissipation via these processes is given by

$$\eta_{\text{diss},i} = \frac{P_{0,i} - P_i}{P_{0,i}} = 1 - \frac{(1 + \sigma_i)(\Gamma_i - 1)}{(1 + \sigma_{0,i})(\Gamma_{0,i} - 1)} \quad (3)$$

(Sikora et al. 2013), where  $P_i$ ,  $\sigma_i$  and  $\Gamma_i$  are values following the dissipation event.

### 2.1 Luminosities

In addition to synchrotron and ERC emission, radiation is produced by the synchrotron-self-Compton (SSC) process and by “external-synchrotron Compton” (ESC) emission, i.e., Comptonization of synchrotron radiation produced in the sheath (spine) by the spine (sheath). Ratios between the luminosities of the various components can be found from the following approximate relations,

$$L_{\text{syn,em},i}/L_{\text{ERC,em},i} \simeq u_{B,i}^{(i)}/u_{\text{ext}}^{(i)}, \quad (4)$$

$$L_{\text{SSC,em},i}/L_{\text{ERC,em},i} \simeq u_{\text{syn},i}^{(i)}/u_{\text{ext}}^{(i)}, \quad (5)$$

$$L_{\text{ESC,em},i}/L_{\text{ERC,em},i} \simeq u_{\text{syn},k}^{(i)}/u_{\text{ext}}^{(i)}, \quad (6)$$

where energy densities measured in the ( $i$ ) jet comoving frame are

$$u_{\text{ext}}^{(i)} = \frac{\zeta L_d}{4\pi r_{\text{bl}}^2 c} \Gamma_i^2, \quad (7)$$

$$u_{B,i}^{(i)} = \frac{L_{B,i}}{\kappa_{B,i} \kappa_{\theta,i} \pi r_{\text{bl}}^2 c (\theta_i \Gamma_i)^2}, \quad (8)$$

$$u_{\text{syn},i}^{(i)} \simeq \frac{L_{\text{syn,em},i}}{2\pi r_{\text{bl}}^2 c (\theta_i \Gamma_i)}, \quad (9)$$

$$u_{\text{syn},k}^{(i)} = u_{\text{syn},k}^{(k)} \Gamma_{12}^2 \xi_k^{(i)}, \quad (10)$$

the magnetic energy flux is

$$L_{B,i} = \frac{\sigma_i}{1 + \sigma_i} P_i = \frac{\sigma_i}{1 + \sigma_{0,i}} \frac{\Gamma_i - 1}{\Gamma_{0,i} - 1} P_{0,i}, \quad (11)$$

$L_d$  is the disk luminosity,  $\theta_i$  is the half-opening angle of jet component  $i$  (see Fig. 1), and the parameters  $\zeta$ ,  $\kappa_{B,i}$ ,  $\Gamma_{12}$ , and  $\xi_k^{(i)}$  are defined as follows:  $\zeta$  is the fraction of the maximal energy density of external radiation as measured in the jet co-moving frame, limited by the geometry and opacity of the matter which reprocesses/isotropizes the radiation of the accretion disk (see Janiak et al. 2015a and refs. therein);  $\kappa_{B,i}$  is the ratio of the magnetic enthalpy to the magnetic energy density ( $\kappa_B = 2$  for a jet with magnetic field dominated by the toroidal component and  $\kappa_B = 4/3$  for chaotic magnetic fields);  $\kappa_{\theta,2} = 1$ ,  $\kappa_{\theta,1} = 1 - (\theta_2/\theta_1)^2$ ;  $\Gamma_{12} = (1 - \beta_1\beta_2)\Gamma_1\Gamma_2$  ( $\sim \Gamma_2/(2\Gamma_1)$  for  $\Gamma_2 \gg \Gamma_1 \gg 1$ ) is the “relative” Lorentz factor between the spine and the sheath; and  $\xi_k^{(i)}$  is the factor by which the radiation produced in the  $k$ -jet is diluted in the  $i$ -jet.

Combination of Eqs. 4-11 gives

$$l_{\text{syn,em},i} = \frac{4l_{B,i}}{\kappa_{B,i} \kappa_{\theta,i} \zeta^2 (\theta_i \Gamma_i)^2 \Gamma_i^2} l_{\text{ERC,em},i}, \quad (12)$$

$$l_{\text{SSC,em},i} = \frac{8l_{B,i}}{\kappa_{B,i} \kappa_{\theta,i} \zeta^2 (\theta_i \Gamma_i)^3 \Gamma_i^4} l_{\text{ERC,em},i}^2, \quad (13)$$

$$l_{\text{ESC,em},i} = \frac{8l_{B,k} \Gamma_{12}^2 \xi_k^{(i)}}{\kappa_{B,k} \kappa_{\theta,k} \zeta^2 (\theta_k \Gamma_k)^3 \Gamma_k^2 \Gamma_k^2} l_{\text{ERC,em},i} l_{\text{ERC,em},k}, \quad (14)$$

where magnetic energy flux and radiation luminosities are normalized to the disk luminosity ( $l_{\dots} \equiv L_{\dots}/L_d$ ). Fixing the model parameters, one can find all emission luminosities by solving a system of two quadratic equations with two unknown variables,  $l_{\text{ERC,em},i}$  and  $l_{\text{ERC,em},2}$ ,

$$l_{\text{ERC,em},i} + l_{\text{syn,em},i} + l_{\text{SSC,em},i} + l_{\text{ESC,em},i} = \epsilon_i p_{0,i}, \quad (15)$$

where  $p_{0,i} = P_{0,i}/L_d$ , and  $\epsilon_i$  is the fraction of the  $i$ -jet power converted to radiation.

Having computed the emitted luminosities, one can calculate the observed luminosities as a function of the angle between the jet axis and the direction to the observer,  $\theta_{\text{obs}}$ ,

$$l_{\text{ERC},i} = \mathcal{A}_{\text{ERC},i} l_{\text{ERC,em},i}, \quad (16)$$

and all remaining spectral components are amplified by a factor  $\mathcal{A}_{\text{iso},i}$ , where the luminosity amplification functions  $\mathcal{A}_{\text{ERC},i}$  and  $\mathcal{A}_{\text{iso},i}$  are given by Eqs. A1 and A2. For jet opening angles  $\theta_i \ll 1/\Gamma_i$  they can be approximated by

$$\mathcal{A}_{\text{ERC},i} = (\mathcal{D}_i/\Gamma_i)^5 \Gamma_i^2, \quad (17)$$

$$\mathcal{A}_{iso,i} = (\mathcal{D}_i/\Gamma_i)^3 \Gamma_i^2, \quad (18)$$

where  $\mathcal{D}_i = [\Gamma_i(1 - \beta_i \cos \theta_{obs})]^{-1}$ . Accuracy of these approximations is illustrated in Fig. A2. The different amplification function for ERC luminosity comes from the fact that the ERC radiation in the jet comoving frame is not isotropic (Dermer 1995). ESC radiation is also anisotropic in the comoving frame, however, because the relative velocity of the spine and sheath flows is only mildly relativistic, this anisotropy is weak and its effect on the luminosity amplification can be ignored.

## 2.2 Frequencies

Assuming that each electron is accelerated once, the injection rate of accelerated electrons is equal to the electron number flux. This gives

$$\dot{N}_{e,i} \bar{E}_{e,i} = \eta_{e,i} \eta_{diss,i} P_{0,i}, \quad (19)$$

where  $\dot{N}_{e,i}$  is the electron number flux,  $\bar{E}_{e,i}$  is the average energy of the accelerated electrons, and  $\eta_{e,i}$  is the fraction of dissipated energy tapped by electrons. Since

$$\bar{E}_{e,i} = \bar{E}_{e,i}^{(i)} \Gamma_i = (\bar{\gamma}_i - 1) m_e c^2 \Gamma_i, \quad (20)$$

we obtain the average Lorentz factor of accelerated electrons

$$\bar{\gamma}_i = \frac{\eta_{e,i} \eta_{diss,i} P_{0,i}}{m_e c^2 \dot{N}_{e,i} \Gamma_i} + 1. \quad (21)$$

Inserting here Eq. 1 with  $\dot{M}_{p,i} = \dot{N}_{p,i} m_p c^2$  and  $\Gamma_{0,i} \gg 1$  gives

$$\bar{\gamma}_i = \eta_{e,i} \eta_{diss,i} \frac{m_p n_p}{m_e n_e} (1 + \sigma_{0,i}) \frac{\Gamma_{0,i}}{\Gamma_i} + 1. \quad (22)$$

Assuming a broken-power-law electron injection function with a break at  $\bar{\gamma}_i$ , one can find that the peaks of different spectral components in  $\nu L_\nu$  are at frequencies (Janiak et al. 2015b)

$$\nu_{ERC,i} \approx \bar{\gamma}_i^2 \mathcal{D}_i^2 \nu_{ext}, \quad (23)$$

where  $\nu_{ext}$  is the average frequency of the dominant external radiation field,

$$\nu_{syn,i} \approx 3.7 \times 10^6 \bar{\gamma}_i^{-2} B_i^{(i)} \mathcal{D}_i, \quad (24)$$

$$\nu_{SSC,i} \approx \bar{\gamma}_i^2 \nu_{syn,i}, \quad (25)$$

$$\nu_{ESC,i} \approx \bar{\gamma}_i^2 \nu_{syn,k}^{(i)} \mathcal{D}_i = \bar{\gamma}_i^2 \Gamma_{12} \nu_{syn,k}^{(k)} \mathcal{D}_i = \bar{\gamma}_i^2 \Gamma_{12} \nu_{syn,k} (\mathcal{D}_i / \mathcal{D}_k), \quad (26)$$

where  $B_i^{(i)} = \sqrt{8\pi u_{B,i}^{(i)}}$ , and

$$u_{B,i}^{(i)} = \frac{l_{B,i}}{\kappa_{B,i} \kappa_{\theta_i} \pi (r_{bl}^2 / L_d) c (\theta_i \Gamma_i)^2}. \quad (27)$$

## 3 RESULTS

### 3.1 Exemplary model

For the purpose of presenting a representative model we will assume that: 1) prior to the dissipation zone the power of the jet per solid angle is constant across the jet; 2) the half-opening angle of the spine is equal to the Doppler angle (i.e.  $\theta_2 \Gamma_2 = 1$ ); and 3) the energy dissipation is dominated by magnetic reconnection. The latter

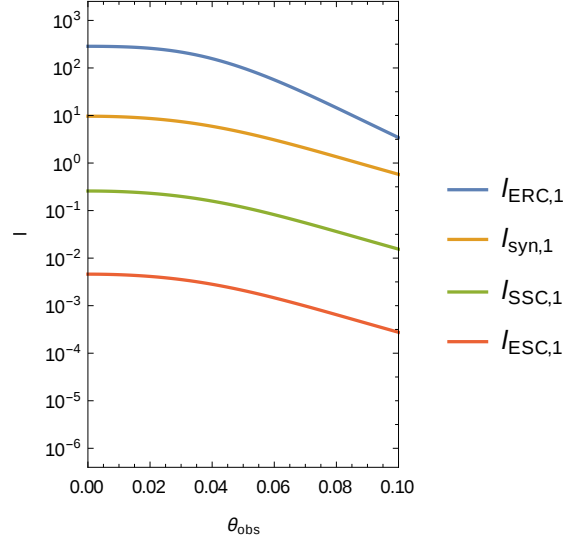


Figure 2. Luminosities normalized by  $L_d$  vs. the observer angle: sheath.

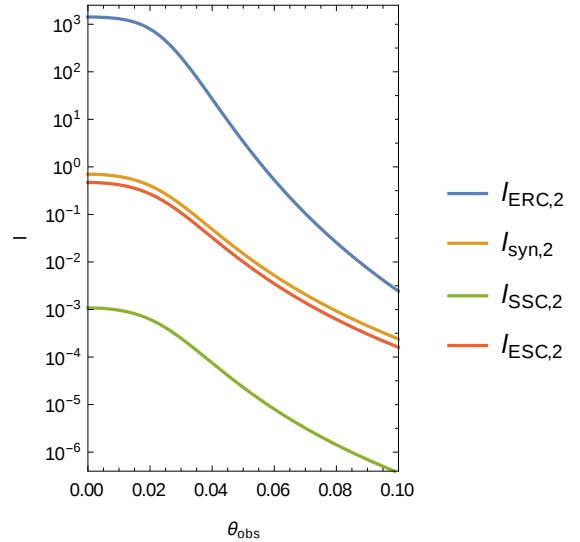


Figure 3. Luminosities normalized by  $L_d$  vs. the observer angle: spine.

assumption allows us to use the approximation  $\Gamma_i = \Gamma_{0,i}$ , whence Eq. 11 gives

$$l_{B,i} = \frac{\sigma_i}{1 + \sigma_{0,i}} p_{0,i}, \quad (28)$$

and from Eq. 3

$$\eta_{diss,i} = \frac{\sigma_{0,i} - \sigma_i}{1 + \sigma_{0,i}}. \quad (29)$$

Figs. 2, 3 and 4 show the apparent luminosities as a function of the inclination angle, calculated for the following set of parameters:  $p_{0,1} = p_{0,2} = 0.5$  ( $\rightarrow (P_0 = P_{0,1} + P_{0,2})/L_d = 1$ );  $\Gamma_1 = 12$ ;  $\Gamma_2 = 48$ ;  $\sigma_{0,1} = \sigma_{0,2} = 1$ ;  $\sigma_1 = \sigma_2 = 0.25$ ;  $\kappa_{B,1} = \kappa_{B,2} = 5/3$ ;

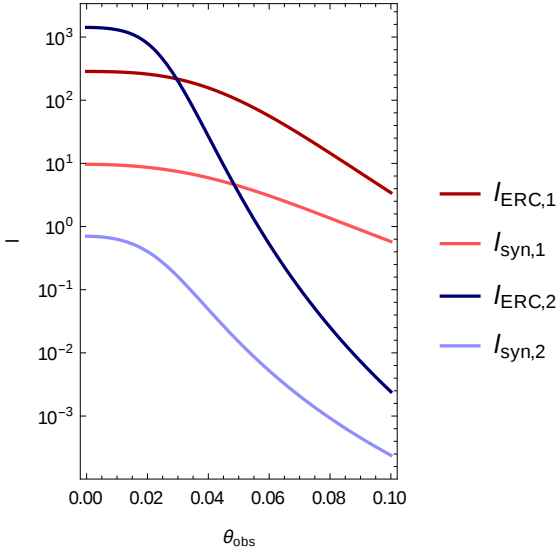


**Figure 4.** ERC and synchrotron luminosities vs. the observer angle.

$\zeta = 0.03$ ;  $\eta_e = 0.5$ ; and  $\eta_{\text{rad}} = 1$  (the latter being confirmed *a posteriori* to be close to unity). In this case  $\epsilon_i \approx \eta_{\text{rad}}\eta_e\eta_{\text{diss},i} \approx 3/16$ . Note that for  $p_{0,1} = p_{0,2}$  and  $\theta_2\Gamma_2 = 1$ , the assumed proportionalities  $p_{0,1} \propto \Omega_1 \propto (\theta_1^2 - \theta_2^2)$  and  $p_{0,2} \propto \Omega_2 \propto \theta_2^2$  imply  $\theta_1 = \sqrt{2}/\Gamma_2$ , i.e. that  $\theta_1\Gamma_1 = \sqrt{2}(\Gamma_1/\Gamma_2)$ . Results presented in Figs. 2, 3 and 4 are obtained using exact formulas for the luminosity amplification factors (see Appendix A). In Fig. 2 the dependence of luminosities of the spectral components produced in the sheath on the observed angle are shown. Since for the sheath the Doppler angle is  $1/\Gamma_1 \sim 0.08$ , that dependence up to  $\theta_{\text{obs}} \sim 5^\circ$  is pretty modest. We can see a clear luminosity hierarchy,  $l_{\text{ESC},1} \ll l_{\text{SSC},1} \ll l_{\text{syn},1} \ll l_{\text{ERC},1}$ , which indicates that Comptonization of the synchrotron luminosity produced in the spine,  $l_{\text{ESC},1}$ , cannot compete with other spectral components at any frequencies. In Fig. 3 the dependence of the spine luminosities on the observed angle are shown. Here the luminosities of all spectral components drop much faster with increasing observed angle; and ERC, SYN, and SSC luminosities are much more separated than the respective sheath luminosities. Another difference is that  $l_{\text{ESC},2}$  is much larger than  $l_{\text{SSC},2}$ , and at  $\theta_{\text{obs}} \sim 1/\Gamma_2$  it can become of order  $l_{\text{SSC},1}$ . In Fig. 4 we compare ERC and SYN luminosities produced in the spine and sheath. Clearly the spine synchrotron luminosity is never important: at  $\theta_{\text{obs}} < 1/\Gamma_2$  the ERC radiation is strongly dominated by the spine and the synchrotron one by the sheath, while at  $\theta_{\text{obs}} > 3/\Gamma_2$  both ERC and synchrotron components are dominated by the sheath.

The dependence of apparent luminosities on model parameters can be easily followed by using the simple analytical approximations obtained under the condition that  $l_{\text{ERC},em,i} \gg l_{\text{syn},em,i} + l_{\text{SSC},em,i} + l_{\text{ESC},em,i}$ . This condition implies  $l_{\text{ERC},em,i} \approx \epsilon_i p_{0,i}$ , and then inserting Eq. 11 into Eqs. 12–14 and multiplying the emitted luminosities by the amplification functions we obtain:

$$l_{\text{ERC},i} \approx \epsilon_i f_i p_0 \mathcal{A}_{\text{ERC},i}, \quad (30)$$

$$l_{\text{syn},i} \approx 4 \frac{c_{\sigma,i} \epsilon_i f_i^2}{\kappa_{B,i} \kappa_{\theta,i} \zeta^2 (\theta_i \Gamma_i)^2} \frac{P_0^2}{\Gamma_i^2} \mathcal{A}_{\text{iso},i}, \quad (31)$$

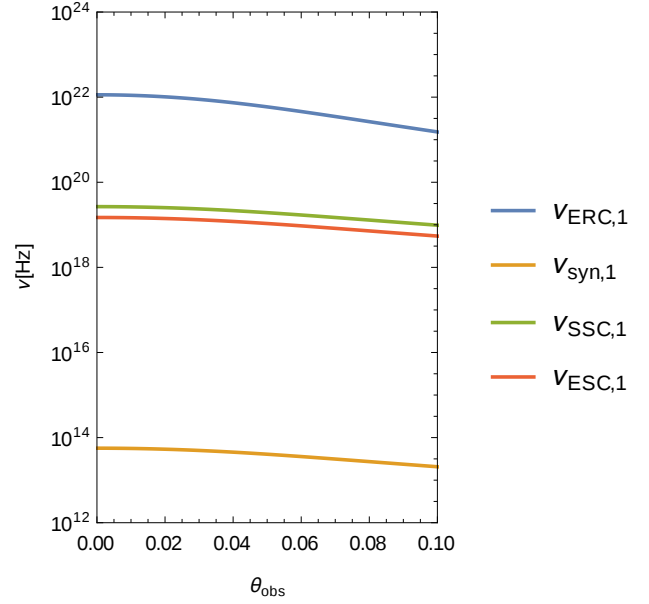


**Figure 5.** Frequencies of the spectral peaks vs. the observer angle: sheath.

$$l_{\text{SSC},i} \approx 8 \frac{c_{\sigma,i} \epsilon_i^2 f_i^3}{\kappa_{B,i} \kappa_{\theta,i} \zeta^2 (\theta_i \Gamma_i)^3} \frac{P_0^3}{\Gamma_i^4} \mathcal{A}_{\text{iso},i}, \quad (32)$$

$$l_{\text{ESC},i} \approx 8 \frac{c_{\sigma,k} \epsilon_i \epsilon_k f_i f_k^2 \Gamma_k^2 \zeta^{(i)}}{\kappa_{B,k} \kappa_{\theta,k} \zeta^2 (\theta_k \Gamma_k)^3} \frac{P_0^3}{\Gamma_i^4 \Gamma_k^2} \mathcal{A}_{\text{iso},i}, \quad (33)$$

where  $f_i = P_{0,i}/P_0$ ,  $c_{\sigma,i} = \sigma_i/(1 + \sigma_{0,i})$ , and  $\theta_1/\theta_2 = f_2^{-1/2}$  as imposed by the condition  $P_1/\Omega_1 = P_2/\Omega_2$ .

The dependence of spectral-peak frequencies of different radiation components on the inclination angle is shown in Figs. 5 and 6. The peak frequencies are calculated assuming  $n_e = n_p$ ,  $\nu_{\text{ext}} = 1.45 \times 10^{14}$  Hz ( $h\nu_{\text{ext}} = 0.6$  eV),  $r_{\text{bl}} = 0.3 r_{\text{sub}}$ , and the sublimation radius for graphite,  $r_{\text{sub}} \approx 1.6 \times 10^{-5} \sqrt{L_d}$  (Sikora et al. 2013 and refs. therein). For the parameters adopted in our exemplary model, Eq. 22 gives  $\bar{\gamma}_i = 690$ , and Eqs. 27 and 28 give  $u_{B,1}^{(1)} = 0.16$  erg cm $^{-3}$  ( $B_1^{(1)} = 2.0$  G) and  $u_{B,2}^{(2)} = 0.017$  erg cm $^{-3}$  ( $B_2^{(2)} = 0.66$  G).

The schematic broad-band SYN-ERC spectra obtained using results of our exemplary models for  $\theta_{\text{obs}} = 1/\Gamma_2$  are illustrated in Fig. 7. This figure illustrates that at very low inclination angles the high energy spectral component is dominated by the ERC radiation produced by the spine, while the low energy spectral components are dominated by synchrotron radiation produced by the sheath.

## 4 DISCUSSION AND CONCLUSIONS

### 4.1 Contamination of optical variations

Lower fractional amplitudes of optical flux variations compared to  $\gamma$ -ray variations, often observed, may result from contamination of variable spine radiation by steady-state or weakly variable sheath radiation. As can be deduced from Fig. 4, such an effect is expected

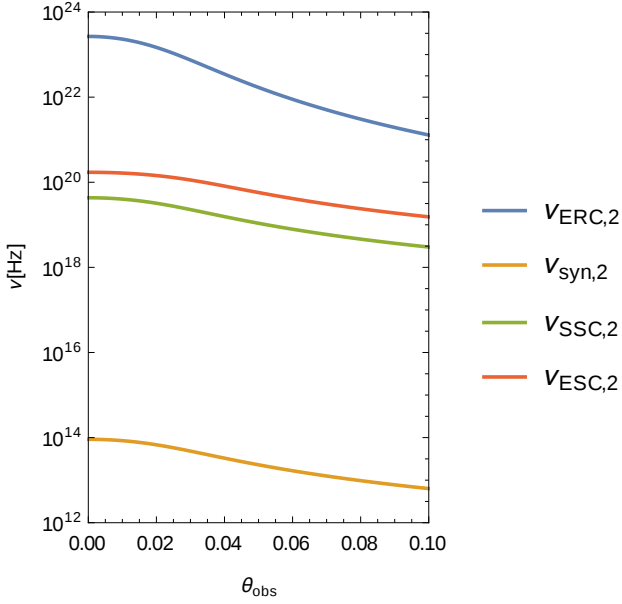


**Figure 6.** Frequencies of the spectral peaks vs. the observer angle: spine.

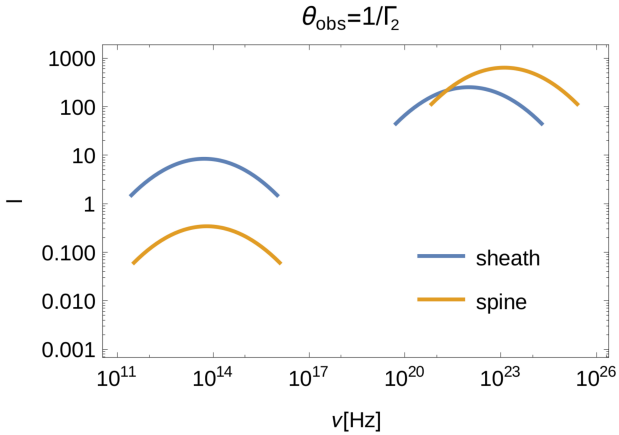


**Figure 7.** The spine and sheath ERC+synchrotron spectra observed at  $\theta_{\text{obs}} = 1/\Gamma_2$ .

to be particularly strong for  $\theta_{\text{obs}} < 1/\Gamma_2$ , for which the observed  $\gamma$ -rays are strongly dominated by the spine.

#### 4.2 $\gamma$ -ray outbursts, their time scales and spectra

The production of powerful  $\gamma$ -ray outbursts can result from a temporal decrease of  $\theta_{\text{obs}}$  due to a change of the spine direction (here,  $\theta_{\text{obs}}$  is defined as measured relative to the instantaneous axis of the wiggling spine). Changes of the spine direction may be caused by current driven instabilities (Nalewajko & Begelman 2012, Janiak et al. 2015a, and refs. therein), or variations of the jet injection direction due to non-axisymmetric interchange instabilities which drive

accretion onto the BH in “magnetically–arrested–discs” (McKinney et al. 2012). In the former case the time scale of the observed outburst is

$$t_{\gamma, \text{flare}} \sim r_{\text{bl}} \Delta\theta_{\text{obs}} / (\mathcal{D}_2 v_A) \quad (34)$$

where  $\Delta\theta_{\text{obs}}$  is the change of the spine direction and  $v_A/c \approx \sqrt{\sigma_{0,2}/(1 + \sigma_{0,2})}$  is the Alfvénic velocity. For our exemplary model parameters this gives  $\Delta t_{\gamma} \sim 5(\Delta\theta_{\text{obs}}/\theta_2)$  days. Hence, a decrease of  $\theta_{\text{obs}}$  from  $1.5\theta_2$  to  $\theta_2$  is followed by an increase in the observed  $\gamma$ -ray flux by a factor 6 (see Fig. A1) with a growth time scale of  $\sim 2.5$  days. In the latter case (variation of the jet injection direction), no local causality constraints apply. Obviously, in the proposed spine-sheath model the observed variability patterns are predicted to be superposed from variations of intrinsic  $\gamma$ -ray production and variations resulting from jet wiggling.

In the proposed spine-sheath model, often-seen hardening of the  $\gamma$ -ray spectrum during powerful outbursts results from the fact that the ERC peak of the spine component is produced at higher frequencies than the ERC peak of the sheath component (see Fig. 7).

#### 4.3 Compton dominance

For observers located at  $\theta_{\text{obs}} < 1/\Gamma_2$ , the high energy component is predicted to dominate over the low-energy component by a factor

$$q \approx \frac{l_{\text{ERC},2}}{l_{\text{syn},1}} = \frac{1}{4} \frac{\epsilon_2 f_2 \kappa_{B,1} [1 - (\theta_2/\theta_1)^2] \zeta(\theta_1 \Gamma_1)^2 \Gamma_1^2 \mathcal{A}_{\text{ERC},2}}{c_{\sigma,1} \epsilon_1 f_1^2 p_0 \mathcal{A}_{\text{iso},1}} \quad (35)$$

which for the parameters of our exemplary model presented in §3 and an observer located at  $\theta_{\text{obs}} < 1^\circ$  is  $\sim 100$  (see Fig. 4). For observers located at  $\theta_{\text{obs}} > 2/\Gamma_2$ , our exemplary model predicts

$$q \approx \frac{l_{\text{ERC},1}}{l_{\text{syn},1}} = \frac{1}{4} \frac{\kappa_{B,1} [1 - (\theta_2/\theta_1)^2] \zeta(\theta_1 \Gamma_1)^2 \Gamma_1^2 \mathcal{A}_{\text{ERC},1}}{c_{\sigma,1} f_1 p_0 \mathcal{A}_{\text{iso},1}}, \quad (36)$$

and for  $\theta_{\text{obs}} > 2^\circ$  gives  $q < 10$ . Since most FSRQs have  $q < 10$  (Giommi, P. et al. 2012; Finke 2013; Lister et al. 2015), most of them are likely to be observed at  $\theta_{\text{obs}} > 2^\circ$ . However, the level of Compton dominance is found to vary in time within individual objects, reaching the largest values during luminous outbursts (see, e.g., Bonnoli et al. 2011; Ackermann et al. 2014; Hayashida et al. 2015).

#### 4.4 Jet energetics

Spine-sheath models are also advantageous for jet energetics. According to one-zone models, the observed  $\gamma$ -ray outbursts with luminosities  $\sim 10^3 L_d$  require jet powers to be  $\sim 100$  times larger than the disk luminosity (Ghisellini et al. 2014). In a spine-sheath model with the observer located at  $\theta_{\text{obs}} < 2^\circ$ , similar  $\gamma$ -ray luminosities are possible with  $P_0 \sim L_d$  (see Fig. 4). Such lower jet energies are supported by observations of blazar radio-halos (Kharb et al. 2010; Meyer et al. 2011).

#### 4.5 Conclusions

Transverse structure in AGN jets, with faster spines/cores and slower sheaths/layers, is indicated by a number of independent observations. On large,  $\sim 100$  kpc scales of powerful double radio sources it is indicated by the fact that jet velocities, inferred from their sideness flux ratios, are barely relativistic ( $\Gamma \sim 1.2 - 1.4$ ; Wardle & Aaron 1997; Mullin & Hardcastle 2009), while X-ray observations suggest  $\Gamma \sim 4 - 14$  (Schwartz et al. 2015). The transverse

kinematic structure of powerful large scale jets is also required to explain details of radio-optical-X-ray spectra of the jet knots (Jester et al. 2006). On parsec and smaller scales, transverse structure is strongly indicated by recent mm-VLBI observations of a jet and a counter-jet in Cyg A (Boccardi et al. 2015). These observations show that the lateral width of the jet is much broader than typical values deduced from blazar studies and that the flow speed drops in the outer layers to mildly relativistic values. Low-power jets, associated with BL Lac objects and their hosts, Fanaroff-Riley Class I (FRI) radio galaxies, also presumably have transverse structure. This is deduced: from edge-brightening of some parsec-scale jets (Giroletti et al. 2004; Nagai et al. 2014); from FRI - BL Lac unification studies (Capetti et al. 2002); and from mildly relativistic speeds deduced from VLBI observations of jets in TeV-BL Lac objects, as contrasted with  $\Gamma \gg 1$  deduced from modeling their broadband spectra (Chiaberge et al. 2000; Piner & Edwards 2014). Additionally, a spine-sheath structure in these objects obviates the need for extremely weak magnetic fields that are implied if one assumes transversely uniform jets (Tavecchio & Ghisellini 2015).

In this paper the spine-sheath jet model is applied to strong-line blazars. We demonstrate that it provides a natural explanation for a number of observed features of  $\gamma$ -ray flares in these objects, including their hardness, their extreme Compton dominance (compared to the optical flux during a flare), and the fact that fractional flux variations in the optical band are often observed to be much weaker than those in  $\gamma$ -rays. And contrary to transversely uniform jets, the production of flares with a large Compton dominance does not require very low jet magnetization. However, the model should be treated as a very crude approximation of a real jet in which the lateral distribution of the Lorentz factor is likely to be a smooth function of angle rather than two-value step-function. This is indicated by recent direct observations of a sub-parsec jet and counter-jet in Cyg A in the mm band (Boccardi et al. 2015). These observations show that the lateral width of the jet is much broader than typical values deduced from blazar studies and that the flow speed drops in the outer layers to mildly relativistic values.

While the Lorentz factors chosen for our exemplary model (§3) were motivated by observations, the relative locations of the  $\gamma$ -ray and synchrotron components in the  $\log \nu L_\nu - \log \nu$  plane (Fig. 7) — also consistent with observations — are determined through physical considerations, by connecting average electron energies with the efficiency of the reconnection process, assuming energetic coupling between electrons and protons, and taking the magnetization parameter  $\sigma$  to be of order unity, as motivated by several theoretical studies (see, e.g., Komissarov et al. 2009; Lyubarsky 2010).

An advantage of our toy model is that it allows one to follow analytically the dependence of different radiation spectral components on the various parameters. In particular, our exemplary model assumptions that  $P_0/\Omega = \text{const}$  and that values of  $\sigma$  and  $\eta_{\text{diss}}$  in the spine and sheath are the same, are rather conservative. Relaxing these assumptions by allowing lower  $\sigma$  and larger  $\eta_{\text{diss}}$  in the spine and/or larger power of the jet in the spine per solid angle may help to explain such extreme events as the one recorded in December 2013 in 3C279 (Hayashida et al. 2015).

Alternative scenarios to explain extreme  $\gamma$ -ray outbursts and their properties have been proposed recently by Asano & Hayashida (2015) and Tavani et al. (2015). Asano & Hayashida consider second-order Fermi acceleration within negligibly magnetized plasma ( $u'_B/u'_e < 10^{-4}$ ). Such a low magnetization seems to contradict theoretical works showing the difficulty of converting initially Poynting flux-dominated flows to  $\sigma \ll 1$  jets (Komissarov

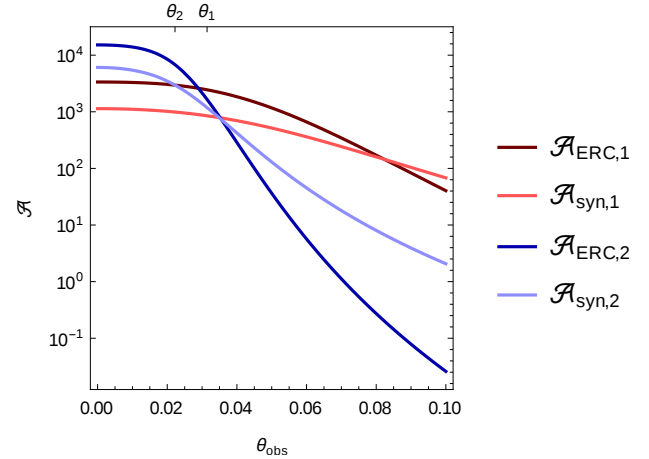


Figure A1. Amplification factors as a function of an observation angle.

et al. 2009; Lyubarsky 2010). Tavani et al. invoke the mirror model (Ghisellini & Madau 1996), assuming that cold mirrors/plasmoids can be formed in the jet, following tearing instabilities in the reconnection layers. However, getting them cold requires very efficient cooling, which is rather difficult to obtain in a jet at thousands of gravitational radii from the BH.

## ACKNOWLEDGEMENTS

The research was supported in part by the Polish NCN grant UMO-2013/08/A/ST9/00795. MCB acknowledges support from NSF grant AST-1411879 and NASA Astrophysics Theory Program grant NNX14AB37G.

## APPENDIX A: LUMINOSITY AMPLIFICATION

$$\mathcal{A}_{\text{ERC},i} = \Gamma_i^2 \frac{1}{\Omega_i} \int_{\phi} \int_{\vartheta_2}^{\vartheta_1} (\delta_i/\Gamma_i)^5 d\Omega, \quad (\text{A1})$$

$$\mathcal{A}_{\text{iso},i} = \Gamma_i^2 \frac{1}{\Omega_i} \int_{\phi} \int_0^{\vartheta_2} (\delta_i/\Gamma_i)^3 d\Omega, \quad (\text{A2})$$

where  $\delta_i = \frac{1}{\Gamma_i(1-\beta_i \cos \vartheta)}$ ,  $d\Omega = d(\cos \vartheta) d\phi$  and  $(\vartheta, \phi)$  are spherical coordinates with z-axis parallel to the direction to the observer. By  $\Omega_i$  we denote total solid angles of jets.

## REFERENCES

- Ackermann M., et al., 2014, *ApJ*, 786, 157  
 Asano K., Hayashida M., 2015, *ApJ*, 808, L18  
 Begelman M. C., Blandford R. D., Rees M. J., 1984, *Rev. Mod. Phys.*, 56, 255  
 Beskin V. S., Nokhrina E. E., 2006, *MNRAS*, 367, 375  
 Boccardi B., Krichbaum T. P., Bach U., Mertens F., Ros E., Alef W., Zensus J. A., 2015, preprint, ([arXiv:1509.06250](https://arxiv.org/abs/1509.06250))  
 Bogovalov S., Tsinganos K., 2005, *MNRAS*, 357, 918  
 Bonning E., et al., 2012, *ApJ*, 756, 13  
 Bonnoli G., Ghisellini G., Foschini L., Tavecchio F., Ghirlanda G., 2011, *MNRAS*, 410, 368

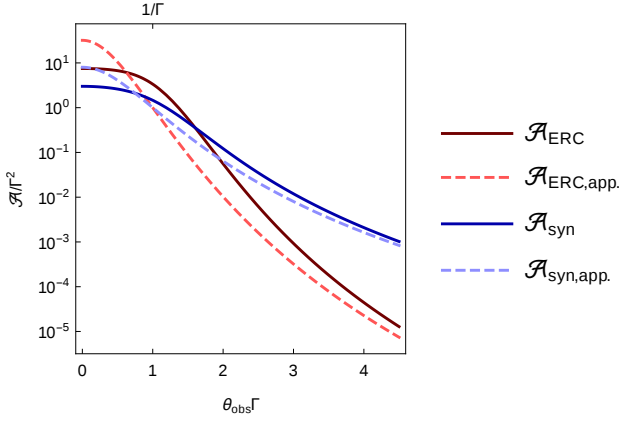


**Figure A2.** Luminosity amplification factors. Solid curves represent factors for a conical jet. Dashed curves represent approximate factors assuming that jet is linear.

Capetti A., Celotti A., Chiaberge M., de Ruiter H. R., Fanti R., Morganti R., Parma P., 2002, *A&A*, **383**, 104  
Carnerero M. I., et al., 2015, *MNRAS*, **450**, 2677  
Celotti A., Ghisellini G., Chiaberge M., 2001, *MNRAS*, **321**, L1  
Chiaberge M., Celotti A., Capetti A., Ghisellini G., 2000, *A&A*, **358**, 104  
Cohen D. P., Romani R. W., Filippenko A. V., Cenko S. B., Lott B., Zheng W., Li W., 2014, *ApJ*, **797**, 137  
D’arcangelo F. D., et al., 2009, *ApJ*, **697**, 985  
Dermer C. D., 1995, *ApJ*, **446**, L63  
Finke J. D., 2013, *ApJ*, **763**, 134  
Ghisellini G., Madau P., 1996, *MNRAS*, **280**, 67  
Ghisellini G., Tavecchio F., Chiaberge M., 2005, *A&A*, **432**, 401  
Ghisellini G., Tavecchio F., Maraschi L., Celotti A., Sbarrato T., 2014, *Nature*, **515**, 376  
Giommi, P. et al., 2012, *A&A*, **541**, A160  
Giroletti M., et al., 2004, *ApJ*, **600**, 127  
Gracia J., Tsinganos K., Bogovalov S. V., 2005, *A&A*, **442**, L7  
Hardee P. E., 2007, *ApJ*, **664**, 26  
Hardee P., Mizuno Y., Nishikawa K.-I., 2007, *Astrophys. Space Sci.*, **311**, 281  
Hayashida M., et al., 2015, *ApJ*, **807**, 79  
Hovatta T., et al., 2014, *MNRAS*, **439**, 690  
Janiak M., Sikora M., Moderski R., 2015a, preprint, ([arXiv:1508.06500](https://arxiv.org/abs/1508.06500))  
Janiak M., Sikora M., Moderski R., 2015b, *MNRAS*, **449**, 431  
Jester S., Harris D. E., Marshall H. L., Meisenheimer K., 2006, *ApJ*, **648**, 900  
Kharb P., Lister M. L., Cooper N. J., 2010, *ApJ*, **710**, 764  
Komisarov S. S., Vlahakis N., K  nigl A., Barkov M. V., 2009, *MNRAS*, **394**, 1182  
Lister M. L., Aller M. F., Aller H. D., Hovatta T., Max-Moerbeck W., Readhead A. C. S., Richards J. L., Ros E., 2015, *ApJ*, **810**, L9  
Lyubarsky Y. E., 2010, *MNRAS*, **402**, 353  
Marscher A. P., et al., 2010, *ApJ*, **710**, L126  
McKinney J. C., Tchekhovskoy A., Blandford R. D., 2012, *MNRAS*, **423**, 3083  
Meyer E. T., Fossati G., Georganopoulos M., Lister M. L., 2011, *ApJ*, **740**, 98  
Mimica P., Giannios D., Metzger B. D., Aloy M. A., 2015, *MNRAS*, **450**, 2824  
Mizuno Y., Hardee P., Nishikawa K.-I., 2007, *ApJ*, **662**, 835  
Mullin L. M., Hardcastle M. J., 2009, *MNRAS*, **398**, 1989  
Nagai H., et al., 2014, *ApJ*, **785**, 53  
Nalewajko K., Begelman M. C., 2012, *MNRAS*, **427**, 2480  
Nishikawa K.-I., Richardson G., Koide S., Shibata K., Kudoh T., Hardee P., Fishman G. J., 2005, *ApJ*, **625**, 60

Piner B. G., Edwards P. G., 2014, *ApJ*, **797**, 25  
Schwartz D. A., et al., 2015, in Massaro F., Cheung C. C., Lopez E., Siemiginowska A., eds, *IAU Symposium Vol. 313*, IAU Symposium. pp 219–224 ([arXiv:1505.06990](https://arxiv.org/abs/1505.06990)), doi:10.1017/S1743921315002215  
Sikora M., Stawarz L., Moderski R., Nalewajko K., Madejski G. M., 2009, *ApJ*, **704**, 38  
Sikora M., Janiak M., Nalewajko K., Madejski G. M., Moderski R., 2013, *ApJ*, **779**, 68  
Sol H., Pelletier G., Ass  o E., 1989, *MNRAS*, **237**, 411  
Tavani M., Vittorini V., Cavaliere A., 2015, preprint, ([arXiv:1510.06184](https://arxiv.org/abs/1510.06184))  
Tavecchio F., Ghisellini G., 2008, *MNRAS*, **385**, L98  
Tavecchio F., Ghisellini G., 2015, preprint, ([arXiv:1509.08710](https://arxiv.org/abs/1509.08710))  
Vercellone S., et al., 2011, *ApJ*, **736**, L38  
Wardle J. F. C., Aaron S. E., 1997, *MNRAS*, **286**, 425  
Wehrle A. E., et al., 1998, *ApJ*, **497**, 178

This paper has been typeset from a  $\text{\TeX}/\text{\LaTeX}$  file prepared by the author.